Numerical investigation into the structure of scalar plumes in a simple room

T. G. Foat*[a, b], S.T. Parker[a], I.P. Castro[b,], Z-T. Xie[b]

[a] Dstl, Porton Down, Salisbury, Wiltshire SP4 0JQ, UK
[b] Faculty of Engineering and the Environment, University of Southampton, Hampshire SO17 1BJ, UK
E-mails: tgfoat@dstl.gov.uk, stparker@dstl.gov.uk, i.castro@soton.ac.uk, z.xie@soton.ac.uk
*Corresponding author

Abstract

Indoor airflow can be complex due to large regions with no dominant flow direction and low velocities. An airborne material released from a surface indoors would be expected to result in a high degree of variability in concentration. It is currently not known how the spatially and temporally resolved concentration field from this type of source could be exploited for the detection of contaminants or vapour from concealed materials. Previous experimental and numerical work has provided information on flow and passive scalar transport in indoor environments but little on how different detection/search strategies could be employed in these environments. This work used large-eddy simulation to extensively study the turbulence fluctuations and the instantaneous vapour field in a widely studied, iso-thermal, benchmark test room, considering the effects of the source size and location. The work provides insight into vapour behaviour within indoor spaces and can have application to fields such as vapour detection, source localisation using autonomous systems, or exposure to toxic chemicals. As an example, we have interpreted the results in terms of current theories of chemical location by animals and the capability of detection dogs.

Keywords: computational fluid dynamics, dispersion, large-eddy simulation, vapour detection, explosives, dog.

Highlights:

- LES has been used to predict concentration from an indoor vapour source
- Concentrations reduce significantly, within a short distance from the source
- Concentrations fluctuate with a frequency that a dog should be able to detect
- Instantaneous concentrations of >28 times the mean concentration were predicted

1. Introduction

Indoor air flows are typically complex due to large regions with no dominant flow direction and low mean velocities. This complexity can be present in both mechanically and naturally ventilated rooms and is accentuated when air change rates are low as secondary drivers of the flow (e.g. temperature gradients) become more important. Indoor flows contain turbulent, laminar and transitional regions [1] and are both unsteady and three-dimensional. This imposes significant challenge for numerical modelling. The concentration field of an airborne material released into such a room is also very complex, particularly if the release is from a constant concentration source (as illustrated by Ferri et al. [2]). In this case the flux would be governed by, amongst other factors, the local flow conditions. A constant concentration source (i.e. one deriving from a surface that has a uniform concentration which is constant in time) release could be representative of evaporation of a pool of liquid, such as a hazardous

chemical, or sublimation of a solid, such as an explosive. This study is focussed on the latter but the results could be applied to other types of constant concentration release.

Indoor air flows have been studied extensively for many years using a range of methods [3], for example: small-scale (e.g. [4]) or full-scale experiments (e.g. [5]), analytical (e.g. [6]), multizone (e.g. [7]), and computational fluid dynamics (CFD) (e.g. [8, 9]) modelling. A range of different turbulence models or modelling methodologies have been shown to perform satisfactorily in appropriate applications [10]. Nevertheless, accurate modelling of turbulence and scalar fluctuations indoors is extremely challenging.

Large-eddy simulation (LES) is a modelling technique in which the large-eddies are resolved and only the small eddies (which are assumed to be isotropic) are modelled. The more commonly used Reynolds averaged Navier-Stokes (RANS) turbulence models have a disadvantage compared to LES, when fluctuating properties are of interest. In RANS, the momentum and scalar transport equations are time averaged and all scales of turbulence and scalar concentration fluctuations are modelled (or parameterised). For the current application, LES was chosen. LES has been used previously to predict the transport of passive scalars in indoor environments. Van Hooff et al. [11] for example compared LES predictions to those from RANS for scalar transport in a simple enclosure. Endregard et al. [12] used LES to study the consequences of the releases of a nerve agent in a large building and Choi and Edwards [13] included the effects of people movement and door opening. These studies focus on time-averaged concentration rather looking to the concentration fluctuations. None of these attempted to relate the time varying concentration to vapour or gas detection and few studies consider extreme concentrations.

Limited experimental data is available for highly spatially and temporally resolved species transport in indoor spaces, and even less for the constant concentration vapour releases which are of major interest to this study. Nevertheless, data of lower spatial and temporal resolution is more readily available. Drescher et al. [14], Cheng et al. [15] and Acevedo-Bolton et al. [17] studied gaseous point releases and monitored concentrations at a limited number of locations. Topp [16] described experiments with evaporation of decane in an indoor environment, but only took a single point measurement. Ferri et al. [2] conducted an experiment using a constant concentration vapour source and measured high resolution time histories of concentration at a number of locations. However, they did not provide any statistics on the turbulent velocity or concentration fluctuations. Hargather et al. [18] sampled vapour from explosives in cargo containers, but only from a single source location. High resolution concentration data from different explosives was produced by Ong et al. [19] using a mass spectrometer. Ong et al. recorded concentration fluctuations from two explosives with durations of approximately 1 s but only at distances up to 0.5 m from the source. High resolution turbulence and fluctuating concentration data is available for some indoor air flow scenarios, such as cross-ventilated rooms [20], but there is additional complexity in these rooms due to the highly unsteady inflow conditions.

Numerous wind tunnel and LES modelling studies have been conducted to investigate concentration plumes in the built environment and in fully turbulent boundary layers [21, 22, 23, 24, 25, 26, 27, 28]. Fackrell and Robins [21] used a wind tunnel to study plumes from ground level and elevated sources. Xie et al. [22] carried out LES modelling of a similar setup and showed good agreement with wind tunnel data. Boppana et al. [24] modelled vapour transport from a constant concentration source within an array of obstacles using LES.

Although the boundary conditions etc. in these studies were different to indoor air flow, the results can still provide a useful comparison.

1.1 Odour location and detection with dogs

Many animals use air or water borne chemical signatures to find and locate targets such as food or mates. Some animals have been trained by humans to track specific targets for purposes such as finding or retrieving game, search and rescue, microbial detection in buildings [29], toxic contamination [30] or detection of explosives [31]. Most frequently these tasks are given to dogs, but others animals such as rats and bees have also been shown to have particular olfactory acuity [32]. Dogs remain the most effective method for detection in many situations, yet there is little understanding of how the complex vapour signature present in indoor spaces affects their ability to detect and search.

The ways in which animals locate the source of a chemical signal include: chemotaxis, movement up a mean concentration gradient [33]; sensing of a chemical followed by anemo- or rheotaxis, moving upwind or upstream [33]; sensing the frequency of odour filaments [34]; and eddy chemotaxis, where the instantaneous concentration signature is used instead of the mean signal [35]. The method, or methods, an animal uses depends on its size relative to the size of the structures in the chemical plume and the nature of the plume i.e. whether it is turbulent, intermittent, laminar or diffusional [34]. Only a subset of these methods may be applicable to an indoor environment where there is often no strong, dominant flow direction. It has not been determined conclusively which of these methods dogs use, but it has been reported, for example, that wind direction can be detected by differential cooling of a dog's nose [33], so they may be able to use anemotaxis. Dogs can also be trained to indicate when they sense the target odour and so move around a space in a structured or random pattern until they find something or complete the search. Source localisation algorithms for autonomous mobile sensors have been developed for indoor environments. One such algorithm, which uses spiral motion with mean and peak concentration measurements, was designed and demonstrated successfully by Ferri et al. [2] using an ethanol vapour source and a tracking robot in a mock-up room.

Dogs are reported to sniff with a frequency of between 4 Hz and 7 Hz [36] and the odour molecules take of the order of 0.1 s to diffuse through the nasal mucus to the epithelial surface [37], thus enabling them to take advantage of the additional information that is present in a fluctuating concentration signal.

Finkelstein et al. [38] carried out measurements of air flows in two different full scale furnished and occupied test rooms with 44 different combinations of air distribution and air exchange rates from 4 h^{-1} to 8 h^{-1}. They took measurements in what was defined as the occupied zone. Time-averaged air velocities from 0.05 $m \cdot s^{-1}$ to 0.6 $m \cdot s^{-1}$ were measured with turbulence intensities, $Ti(\bar{u})$, of up to 70% at the lower velocities and not lower than 10% for all velocities. $Ti(\bar{u})$ is defined as $u_{RMS}/\bar{u}$, where u_{RMS} is the root mean square (RMS) velocity and $\bar{u}$ is the mean velocity. 90% of the velocity fluctuations (by energy) were between 0.1 Hz and 2 Hz in the occupied zone. Concentration fluctuations for a chemical with a Schmidt number (the ratio of momentum diffusivity to mass diffusivity), *Sc*, close to unity, in the same rooms, would be expected to have a similar frequency range and so these fluctuations should be detectable by dogs when sampling at up to 7 Hz.

In order to be able to determine how dogs find odour sources in indoor environments, or to be able to offer advice on how training methods or operational procedures could be improved, an

understanding of spatially and temporally varying vapour concentration in indoor environments is required.

The principle aim of this study is to investigate and understand the unsteady and three-dimensional flow present in rooms and the extent to which it can produce complex vapour fields that could either help or hinder vapour detection. The intention is to illustrate some of the key features of these vapour fields to raise the awareness of people conducting either training or operational detection activities.

2. Methodology

2.1 Indoor geometry

In order to understand the temporally and spatially varying vapour concentration field that a detection dog may be exposed to in an indoor environment, a CFD model has been built of a test room. This scenario is based on the widely studied benchmark test case of Nielsen [39]. This test case was used because it is well documented and allows for validation of the mean velocity and RMS velocity, although clearly it is not representative of all rooms. Even in this simple room the flow is unsteady, three-dimensional and extremely complex. The simple geometry allows vigorous CFD modelling of plumes from vapour sources to be performed and could provide sufficient information to assess RANS modelling approaches. The Methods developed in this work could be applied to more complex rooms in the future. Vapour sources were located on the floor, to the left of the room where the flow is slower and to the right where the flow was faster and steadier (see Fig. 2). Two different size sources were defined at each location. These are described in more detail in Section 2.2.1.

Fig. 1 shows the room geometry, with room dimensions L = 9 m, H = W = 3 m, inlet slot height, h = 0.168 m and outlet slot height, t = 0.48 m. The test case was created for the testing of two-dimensional CFD codes [39], with the assumption that with $W >> H$, the flow would be two-dimensional. However, laser-Doppler anemometer data is provided from a scale model experiment with $W = H$ [4]. The mean inlet velocity u_0 = 0.455 $m \cdot s^{-1}$ and the temperature = 20°C. The air change rate (ACR) is defined as Q / V where Q is the volumetric flow rate at the inlet and V is the room volume. For this room, the ACR is 10 h^{-1}. Based on a dynamic viscosity, μ = 1.84 x 10^{-5} $m^2 \cdot s^{-1}$ and an air density, ρ, of 1.20 $kg \cdot m^{-3}$, the inlet

Reynolds number, *Re* was 5000, with *h* as the characteristic dimension.

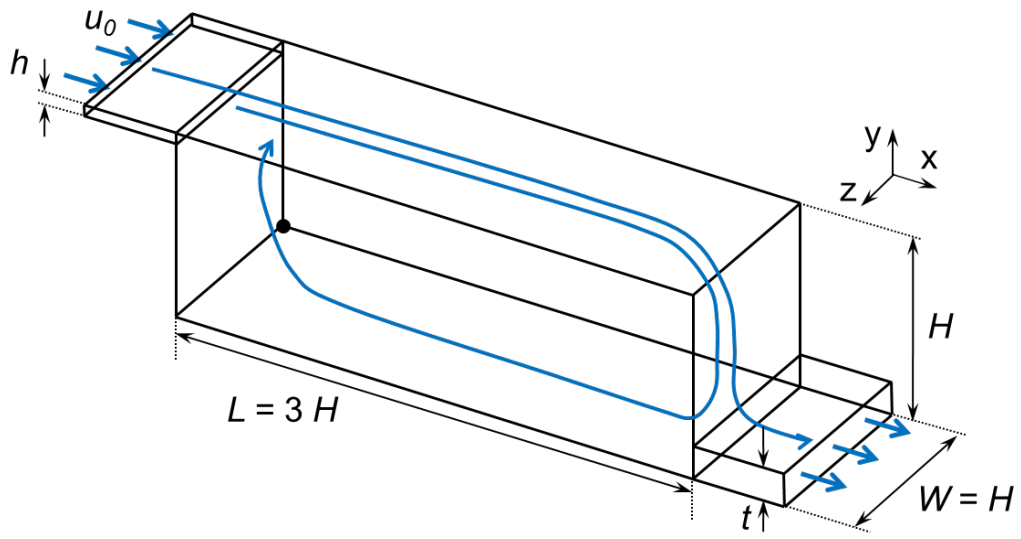

Fig. 1. The Nielsen benchmark test case. The blue arrows indicate the mean flow direction and the black dot is located at axis origin. For the current modelling both the inlet and outlet channels were 10*h* long.

A number of studies have modelled the flow in the Nielsen benchmark test case using either a two or three dimensional RANS approach, e.g. [40, 41, 42, 43, 44, 45]. The studies showed significant variation in results when applying different turbulence models, e.g. a change in the overall flow pattern and other features such as an under-prediction of turbulence intensity [51]. A smaller number of papers discussed application of LES, e.g. [46, 47, 48, 49], but did not include species transport. Lattice Boltzmann methods have also been used [50] with some success. Nielsen et al. [51] commented that it is possible that different flow patterns were present in the experiment but were not measured. Nielsen et al. [51], Thysen [45] and Voigt [52] also commented on the possible three-dimensionality of the mean flow field.

2.2 CFD

In this work ANSYS® Fluent® V15.0 (hereon referred to as Fluent) was used to model the flow and vapour transport with an LES approach, using a structured mesh produced in Gambit™ V2.4. For LES, the filtered Navier-Stokes equations (shown in tensor notation, Eq. 1 were solved.

$$\rho\left[\frac{\partial \widetilde{u_i}}{\partial t}+\frac{\partial}{\partial x_j}\left(\widetilde{u_i}\widetilde{u_j}\right)\right]=-\frac{\partial \tilde{p}}{\partial x_i}+\frac{\partial}{\partial x_j}\left(\mu\frac{\partial \widetilde{u_i}}{\partial x_j}-\tau_{ij}\right) \quad (1)$$

A tilde represents a filtered variable, u_i and x_i are the velocity and direction respectively, t is the time, p is the pressure and τ_{ij} is the subgrid stress tensor. The dynamic Smagorinsky model, typically applied to indoor airflows [11, 46], was used to calculate $\tau_{ij,}$ using the following.

$$\tau_{ij}=-2\mu_{sg,t}\widetilde{S_{ij}}+\frac{1}{3}\tau_{kk}\delta_{ij}, \quad (2)$$

$$\mu_{sg,t}=\rho C_{DS}\Delta^2\left|\tilde{S}\right|, \quad (3)$$

where $\mu_{sg,t}$ is the subgrid turbulent viscosity, S_{ij} is the strain rate tensor, δ_{ij} is the Kronecker delta, C_{DS} is the dynamic Smagorinsky model constant, Δ is the LES filter size, which is the cube root of the cell volume, and $\tilde{S}$ is $\sqrt{2\widetilde{S_{\iota J}}\widetilde{S_{\iota J}}}$. C_{DS} is calculated by resolving the flow field over the original LES filter size and a test filter which is double the width of the LES filter. It should be noted that C_{DS} is equivalent to the square of the standard Smagorinsky constant, C_S. Fluent clips $\sqrt{(C_{DS})}$ at zero and 0.23. The volume averaged value for $\sqrt{(C_{DS})}$ in the current model was 0.14.

The vapour was modelled as a passive scalar using the filtered scalar transport equation.

$$\rho\left[\frac{\partial\tilde{c}}{\partial t}+\frac{\partial}{\partial x_j}(\widetilde{u_\iota}\tilde{c})\right]=\frac{\partial}{\partial x_j}\left[\left(D_{sg,t}+D_m\right)\frac{\partial\tilde{c}}{\partial x_j}\right], \quad (4)$$

where c is the concentration, $D_{sg,t}$ is the subgrid turbulent diffusivity and D_m is the molecular diffusivity. $D_{sg,t} = \mu_{sg,t} / (\rho\, Sc_{sg,t})$, where $Sc_{sg,t}$ is the subgrid turbulent Schmidt number. A dynamic scalar flux model [53], as used and validated in a number of LES scalar dispersion studies [54, 55], was used to calculate $Sc_{sg,t}$. Fluent clips $Sc_{sg,t}$ at 0.1 and 10.

The flow was initialised using results from a steady k-ε Renormalization Group (RNG) turbulence model. The LES model was run using Fluent's non-iterative time advancement scheme [53]. The time step, Δt, was 0.01 s and the non-dimension time step, $\Delta t / \tau$, (where τ = 1 / ACR = 353 s) was 2.83 x 10^{-5}. This time step resulted in a Courant–Friedrichs–Lewy (CFL) number of ≤ 0.5 across the bulk of the domain with a few small regions having a slightly larger CFL number but still below 0.76. For the LES solution, a second order central difference scheme (CDS) was used for the momentum transport terms with a 'pressure implicit with splitting of operator' (PISO) scheme used for the pressure-velocity coupling. The species transport equations were solved using Fluent's bounded central difference scheme [53]. The species transport equations were initially also solved using a CDS. No instability was observed in the flow field but it was apparent in the species field in the form of intermittency that appeared to be non-physical. It is believed that the species transport became unstable, whereas the momentum transport did not, due to the presence of large concentration gradients. The flow was run until mean velocities stabilised (2τ in this case) and then averaged for at least 4τ. The vapour sources were turned on once the flow was developed and the species field was then initialised for at least 4τ and averaged for 10τ. It was found that the longer averaging period, compared to the velocity field, was required due to the additional unsteadiness of the vapour field.

A boundary condition which is representative of the unsteady turbulence at the inlet is typically required for LES and this can be achieved in a number of ways [56, 57]. Fluent's vortex generation method [53] was used in this case, as in other indoor LES studies [11]. The velocity, turbulent kinetic energy and dissipation rate profiles at the inlet were taken from a separate steady k-ε RNG model in which the flow was allowed to develop in a channel which was h high, H wide and 30 h long. The mean inlet velocity for the sub-model, u_0, was set to that defined by Nielsen [39]. The hydraulic diameter for the sub-model, D_H, used to define the

integral length scale at the inlet, was calculated using an equation for rectangular ducts [11, 58], $D_H = 4Wh / 2(W + h) = 0.318$ m. The turbulent kinetic energy decayed rapidly in the inlet channel so a turbulence intensity, $Ti(u_0) = u_{RMS}/u_0 = 4.6\%$, was achieved at the end of the inlet channel, i.e. at the entrance to the main volume of the domain, while a value of $Ti(u_0) = 8.4\%$ was reported by Nielsen [39]. It was noticed that the vortex generation method only affected the velocity and RMS velocity profiles close to the top wall within a distance of approximately H from the end of the inlet channel, compared to those without inflow turbulence generation. All walls were given no-slip boundary conditions.

A fully structured hexahedral mesh with 5.4 million cells was produced initially. A high-resolution image of the mesh on the vertical centre plane and a horizontal plane at a distance of h / 2 from the floor is provided in the supplementary material (mesh-vertical-centre-plane.tif & mesh-horizontal-plane.tif). There were 20 cells across the inlet height and the largest cell dimension in the domain was 0.03 m. The initial mesh was refined near the source locations and also around the shear layer of the wall jet. Nearly all the cells on the top and left/right walls ($x / H = 0$ and 3) had a y_1^+ (where y_1^+ is the non-dimensional distance from the wall of the first cell centre) of less than 5. As a result the first cell centres were in the viscous sub-layer. The near wall mesh on the sides ($z / H = 0$ and 1) was slightly coarser, with y_1^+ as high as 7.5 near the inlet. Most of the mesh on the bottom wall had $y_1^+ < 2.5$ and the source regions had a y_1^+ of 0.6 and1.7 for the left and right sources respectively. The mesh dependency is discussed in Section 2.3.

The ratio of subgrid scale turbulent kinetic energy (TKE) to total TKE can be used to give an indication of the amount of turbulence that is being resolved, as opposed to modelled, in an LES simulation [59]. For the initial mesh the volume weighted average ratio was 1.5%, showing that the mesh size was sufficiently small to resolve 98.5% of the TKE. Abdilghanie et al. [60] reported that their LES mesh was well resolved with a TKE ratio of less than 5% across most of their domain.

2.2.1 The vapour source and monitoring locations

This paper focuses on vapour released from trinitrotoluene (TNT) explosive but the results could be applied to most materials which act as a constant concentration, area, vapour source. These materials can be viewed as vapour generators with the production rate being a function of physicochemical factors (e.g. vapour pressure and molecular vapour-air diffusion coefficient), scenario details (source size, ambient conditions, local air flow and ventilation) or internal processes such as the diffusion of a vapourising compound through the solid. The CFD models used to study the vapour transport are based on passive scalar transport and it is assumed that the concentrations can be scaled linearly to represent different target vapours. Processes such as vapour sorption onto surfaces, which may make the scaling non-linear, have not been included.

The movement of a dog and handler in the room has not been accounted for and it is expected that this movement would produce additional unsteadiness and increased local mixing.

Two sets of large and small vapour sources were modelled representing the source material fully exposed on the floor of the room. The large and small sources were defined as squares with side length, d, of 0.144 m and 0.048 m respectively. The areas, A, of the large and small sources were 0.0207 m^2 and 0.00230 m^2 respectively, therefore, the large source was nine times the small source. The source face was set with a species mass fraction, c_0, which was uniform across the area of the source and constant in time. This creates a vapour source based on the assumption that, close to the surface of the material, there is a continuous reservoir of vapour at the saturation vapour pressure concentration. This assumption is a reasonable one when the flow over the source is weak, but, too high a flow could deplete this reservoir faster than it is replenished from the bulk material. For semi-volatile organic compounds (SVOCs) such as TNT, the vapour production rate should only be limited by processes external to the solid [61].

Both sets of sources were centred in the z direction with the centre of one at x = 0.350 m and the other at x = 7.572 m (Fig. 2). This placed the left sources in a small recirculation region where the mean velocity was small and in the positive x direction (see Fig. 5). The right sources were in a faster flowing region with flow in the negative x direction. The left source location is perhaps more representative of typical mechanically or naturally ventilated rooms which would not be expected to have strong directional flow near the floor.

Fig. 2 shows the locations of the monitor points and lines used to report vapour concentrations. Vertical lines VR2 and VR3 were used to show how the concentration profiles evolve downwind of the source. As the flow direction near the left sources varies it was not possible to define a downwind direction to the same extent so additional vertical monitor lines for the left sources were not used.

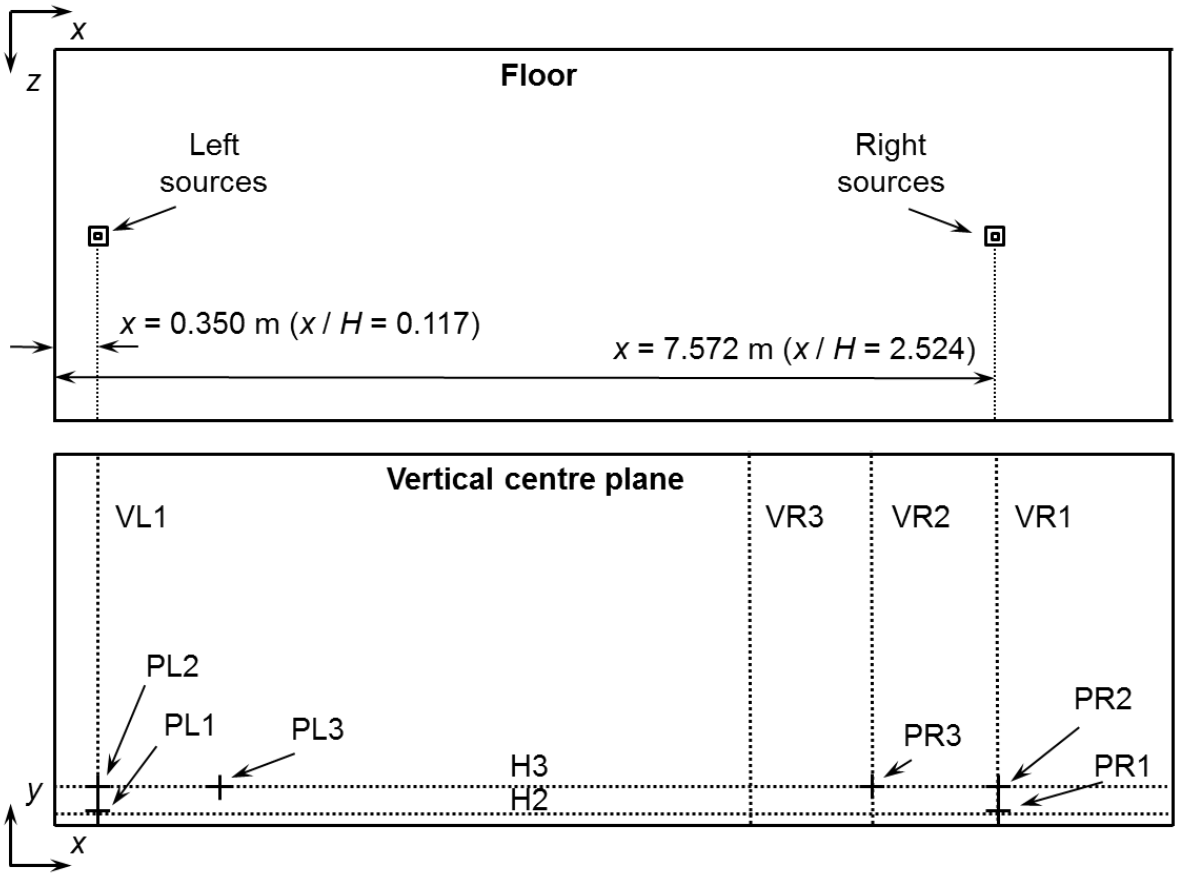

Fig. 2. The locations of the sources, monitor lines and monitor points on the floor (upper) and the vertical centre plane (lower). Lines VL1 and VR1 are centred on the left and rights sources respectively. Lines VR2 and VR3 are offset from VR1 by 1 m and 2 m respectively. Lines H3 and H2 are 0.3 m and 0.084 m above the ground respectively. There is an additional horizontal line, H1, at y = 0.01 m which is not shown here. Points PL1 and PL2 are 0.1 m and 0.3 m above the centre of the left sources and PR1 and PR2 are at the same heights above the right sources. Points PL3 and PR3 are at y = 0.3 m and are offset from the centre of the sources in the x-direction by 1 m. All points and lines are on the vertical centre plane.

The vapour had a diffusion coefficient, D_m, of 5.6 x 10^{-6} $m^2 \cdot s^{-1}$ which is representative of the diffusion of TNT vapour in air under ambient conditions [62], the Schmidt number, Sc = 2.7. The volatility of TNT at 20°C is 3.2 x 10^{-8} $kg \cdot m^{-3}$ (or 3.4 parts per billion, volume/volume) [63].

2.3 Mesh, time step size and subgrid scale model sensitivity

To assess the mesh dependence of the model, separate adaptions were made on a test model to study the effect on both the flow field and the vapour flux from the source. As the ratio of the estimated subgrid scale TKE to total TKE was already small across most of the domain, the mesh was only refined in the inlet channel and the start of the shear layer when testing the effect of the mesh on the flow field. See supplementary material files for an image of the inlet and shear layer refined mesh (mesh-vertical-centre-plane-refined-inlet.tif). For the refined mesh, Δt was reduced to 0.005 s to maintain the same maximum CFL number in the inlet region. The refinement of the mesh in the inlet channel and shear layer had little effect on the

velocity and RMS velocity profiles, so this refinement was not used for subsequent modelling.

Two localised adaptions of the fully structured mesh at the left and right source locations were performed to assess the dependence of the vapour flux predictions on the mesh. The mesh was refined in a cuboid (0.6 m x 0.6 m x 0.6 m in the *x*, *y* and *z* directions respectively) centred on the sources to produce the first adaption and then refined again in a smaller region (0.3 m x 0.3 m x 0.3 m in the *x*, *y* and *z* directions respectively). See supplementary material files for images of the refined meshes (mesh-vertical-centre-plane-refined-left.tif and mesh-vertical-centre-plane-refined-right.tif). Considering only the convective component, the vapour flux, F [kg·m^{-2}·s^{-1}], given by Eq. (5), was compared for each mesh.

$$F = \frac{\int \bar{u}\bar{c}\rho \, dA_{outlet}}{A}, \tag{5}$$

where $\bar{c}$ is the time average concentration, A_{outlet} is the area of the domain outlet and A is the area of the source. Eq. (5) should approximate the flux at the source with a good accuracy (when averaged over a sufficiently long period), given that the turbulent flux is usually small compared to the streamwise convective component [11].

For both source locations there was a small change in the vapour flux as the mesh was refined but this was never more than an 8% difference, compared to the initial mesh, for the left sources and never more than a 2% difference for the right sources. The overall patterns in the mean and RMS vapour fields were qualitatively similar for all three meshes, as were the mean and RMS velocities. In addition, Boppana et al. [24] showed that reducing y_1^+ from 2.1 to 1.1 at their constant concentration vapour source had little effect on the local mean concentration when normalised to the vapour flux, for naphthalene (Sc = 2.3). As the variation in flux for the right sources was small and the initial mesh had a y_1^+ within the range used by Boppana et al., the initial mesh was used for modelling the right sources. As the variation in flux for the left source was larger, the mesh with one refinement was used for subsequent modelling. This meant that y_1^+at the left and right sources was 0.3 and 1.7 respectively.

Using the mesh with one refinement at the left source, Δt, was reduced from 0.01 s to 0.005 s. This change had minimal effect on the velocity and RMS velocity profiles. With the reduction in Δt, the flux from the small and large left sources increased by 4% and 3% respectively. The concentration and RMS concentration fields were similar for both time step sizes. As the results showed little time step size dependency, Δt = 0.01 s was used to produce the results shown in Section 3.

2.4 Validation

The results were validated through comparison of: the mean and RMS velocity to experimental data [39] (see Section 3.1), the vapour flux to a model for vapour emission [64] (see Section 3.2) and the RMS concentrations with wind tunnel and LES studies of ground level passive scalar releases in a fully turbulent boundary layer [21, 22, 28] (see Section 3.2).

3. Results

3.1 Validation of the flow field

Time-averaged velocity vectors on the vertical plane are shown in Fig. 3. The flow is dominated by a large primary recirculation with secondary recirculation regions in the lower left (small *x* and small *y*) and upper right (large *x* and large *y*) corners. Fig. 3 shows that TKE,

created in the shear layer produced by the wall jet, decays as the jet moves along the top wall and down into the room.

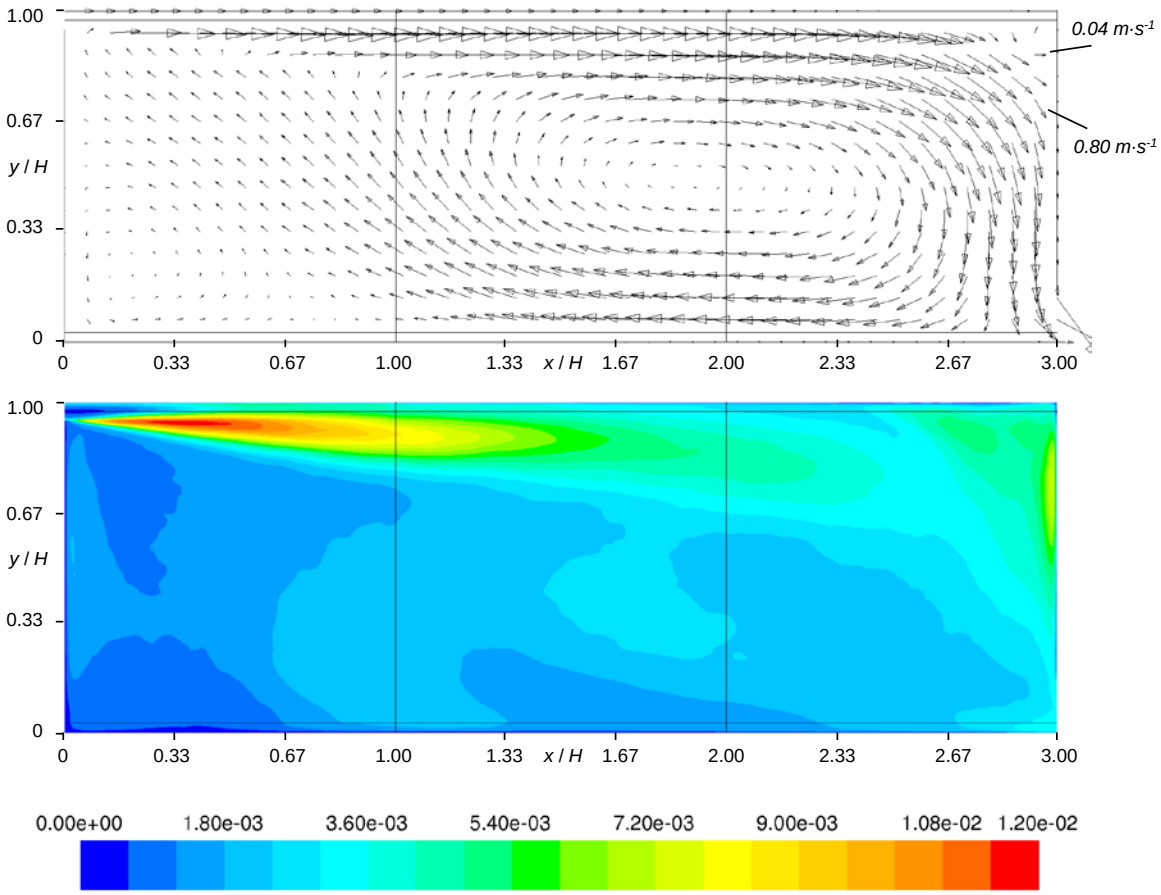

Fig. 3. Mean velocity vectors (upper) and contours of resolved TKE [$m^2 \cdot s^{-2}$] (lower), on the vertical centre plane. The vertical lines are at $x / H = 1$ and 2 and the horizontal lines are at $h / 2$ from the top wall and $h / 2$ from the bottom wall. Vectors are plotted on a regular grid of points and some example vectors are annotated.

The time-averaged velocity, $\bar{\boldsymbol{u}}$, and u_{RMS}, both normalised against u_0, were compared to the data of Nielsen [39] and the results are shown in Fig. 4 and Fig. 5. The figures show data over vertical lines on the centre plane at $x / H = 1$ and 2 and on horizontal lines on the centre plane at a distance of $h / 2$ from the top and bottom surfaces (as shown in Fig. 3).

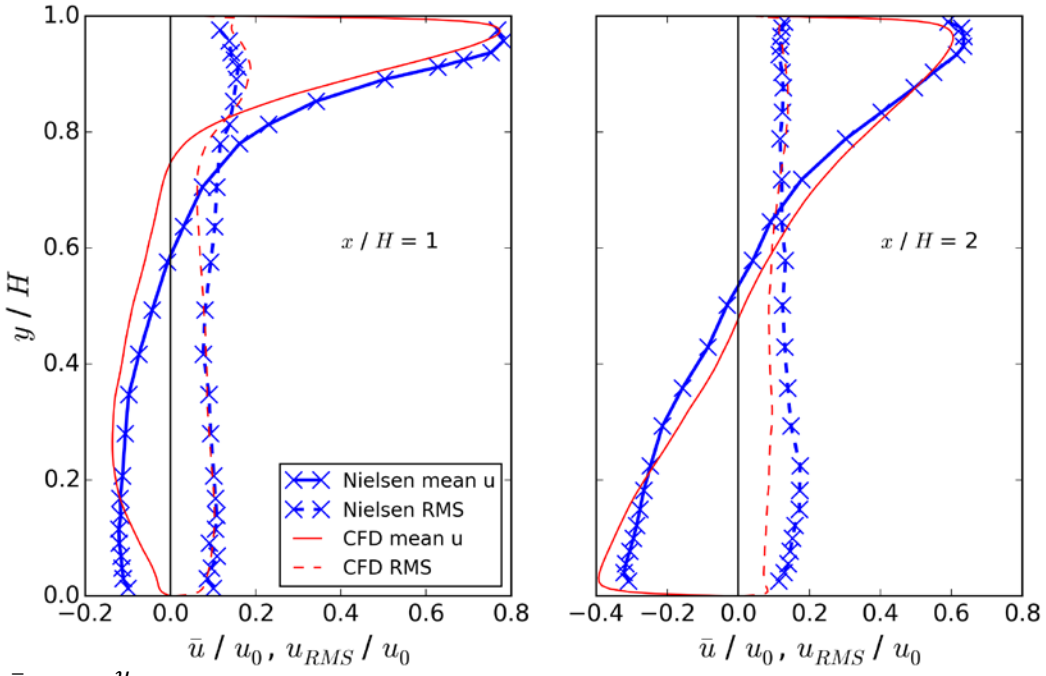

401
402 Fig. 4. $\bar{u}/u_0$ and u_{RMS}/u_0 against y / H on vertical lines on the centre plane at $x / H = 1$ (left graph) and $x / H = 2$
403 (right graph).

404

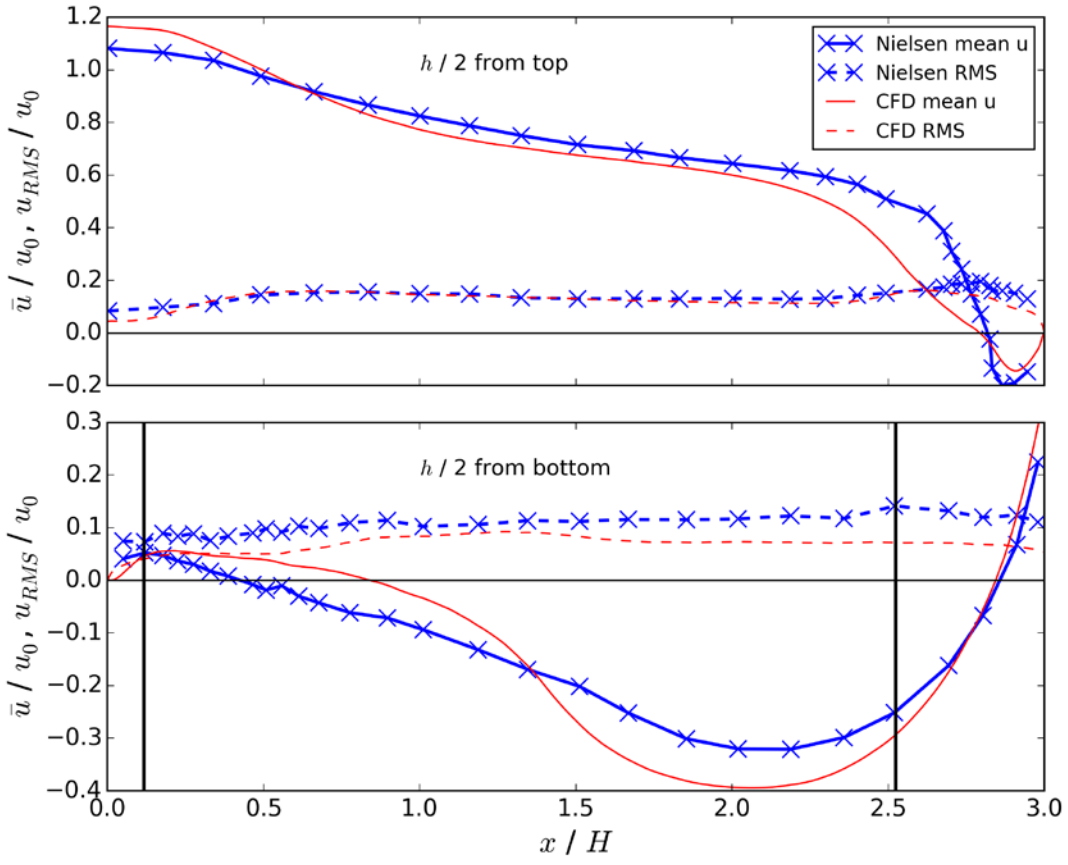

405

Fig. 5. $\bar{u}/u_0$ and u_{RMS}/u_0 against x / H on horizontal lines on the centre plane at a distance of h / 2 from the top wall (upper graph) and h / 2 from the bottom wall (lower graph). The vertical lines show the locations of the source centres.

The mean and RMS velocity profiles are broadly similar to those reported by, for example [42, 45, 49]. Interestingly the velocity prediction in the present study at x / H = 1 are similar to those of Davidson [46], who used a considerably coarser mesh. The main discrepancies between the LES model and the experiment are: the velocity profile near the floor, in particular the point of separation and the peak negative velocity; and the under-prediction of the RMS velocity near the floor. Regarding the former, some previous modelling studies [45, 46] have shown a better fit to the mean velocity data near the floor. However, a similar point of separation to that shown in the current modelling, was reported by Pedersen and Meyer [65], who carried out particle image velocimetry measurements in a scale model. The flow in the present model could be made to follow the experiment profile near the floor much closer if a small asymmetric flow was applied at the inlet. The under prediction of the RMS velocity near the floor is a feature that, to the authors' knowledge, has not been predicted accurately in any published studies. Zhang [49] stated that coarse mesh resolution may have been the cause of their errors in the LES prediction of the fluctuating velocity. However, the finer mesh used in the present study has not significant altered the effectiveness of the model.

The model performance has been assessed using a number of metrics as described by Hanna et al. [66] and used for velocities and turbulence predictions by Tominaga et al. [67] and van Hooff et al. [68]. These are: the percentage of points within a factor of two (FAC2), the percentage of points within a factor of 1.3 (FAC1.3), the fractional bias (FB) and the normalised mean square error (NMSE). Each assessment used 106 data points. The results are presented in Table 1, alongside the ideal values for each metric for a perfect model.

	$\bar{u}/u_0$	u_{RMS}/u_0	Ideal values
FAC2	0.75	0.95	1
FAC1.3	0.53	0.51	1
FB	0.14	0.22	0
NMSE	0.26	0.11	0

Table 1. Model performance metrics for $\bar{u}/u_0$ and u_{RMS}/u_0.

The metrics show that the model has performed well in predicting both the mean and RMS velocities, with more than 50% of predictions within a factor of 1.3 of the experimental data.

It is of interest to note that the turbulence intensity, $Ti(\bar{u})$, was very high across the domain, as is typical of indoor air flows. The median $Ti(\bar{u})$ on the vertical line at x / H = 1 was 77% and on the horizontal line, at a distance of h / 2 from the bottom wall, it was 85%.

3.2 Vapour concentration

The predicted vapour fluxes, F, calculated using Equation (1), for the large and small sources at both locations for TNT are given in Table 2. The table shows the fluxes predicted by the CFD model compared to those from a model of Danberg [64] for emission from a rectangular source. The Danberg model is given by the following.

$$Sh = 0.796 \left(\frac{u^* d}{\nu}\right)^{2/3} Sc^{1/3}, \quad (6)$$

where *Sh* is the Sherwood number, u^* is the friction velocity and *d* is the distance across the source in the streamwise direction.

	Left		Right	
	Small	Large	Small	Large
CFD flux	37.1	25.7	71.4	49.9
Danberg flux	28.4	19.5	54.9	38.1
Ratio CFD:Danberg	1.3	1.3	1.3	1.3

Table 2. Vapour flux [ng·m^{-2}·s^{-1}] predicted by the CFD model compared to those from the Danberg [64] model.

For both source locations, the vapour flux, *F*, from the large source was 0.7 times that from the small source. Therefore, the mass flow rate from the large sources was 6.3 times than from the small source. The fluxes, *F*, from the right sources were 1.9 times those from the left sources (for both sizes). The CFD predictions are very close to those of the Danberg model for all sources. It should be noted that the Danberg model was developed for a steady two-dimensional flow with a constant friction velocity in space and time. This provides additional confidence in the accuracy of the CFD vapour model.

Fig. 6 shows contours of time-averaged concentration, $\bar{c}$, normalised by c_0, on the vertical centre plane, for the left and right large sources. For the left source, there is a small, high concentration region to the right of the release location due to the mean flow in that area being in the positive *x* direction. The vapour is then carried up and round in a clockwise direction. There is a gradient in the mean concentration field towards the lower left of the domain where the source is located. However, this gradient is very weak on the right side of the room. For the right source the high concentration region stays close to the floor and there is a gradient in from the lower left of the room to the lower right. Similarly to the left source, the concentration gradients are weak in large parts of the room.

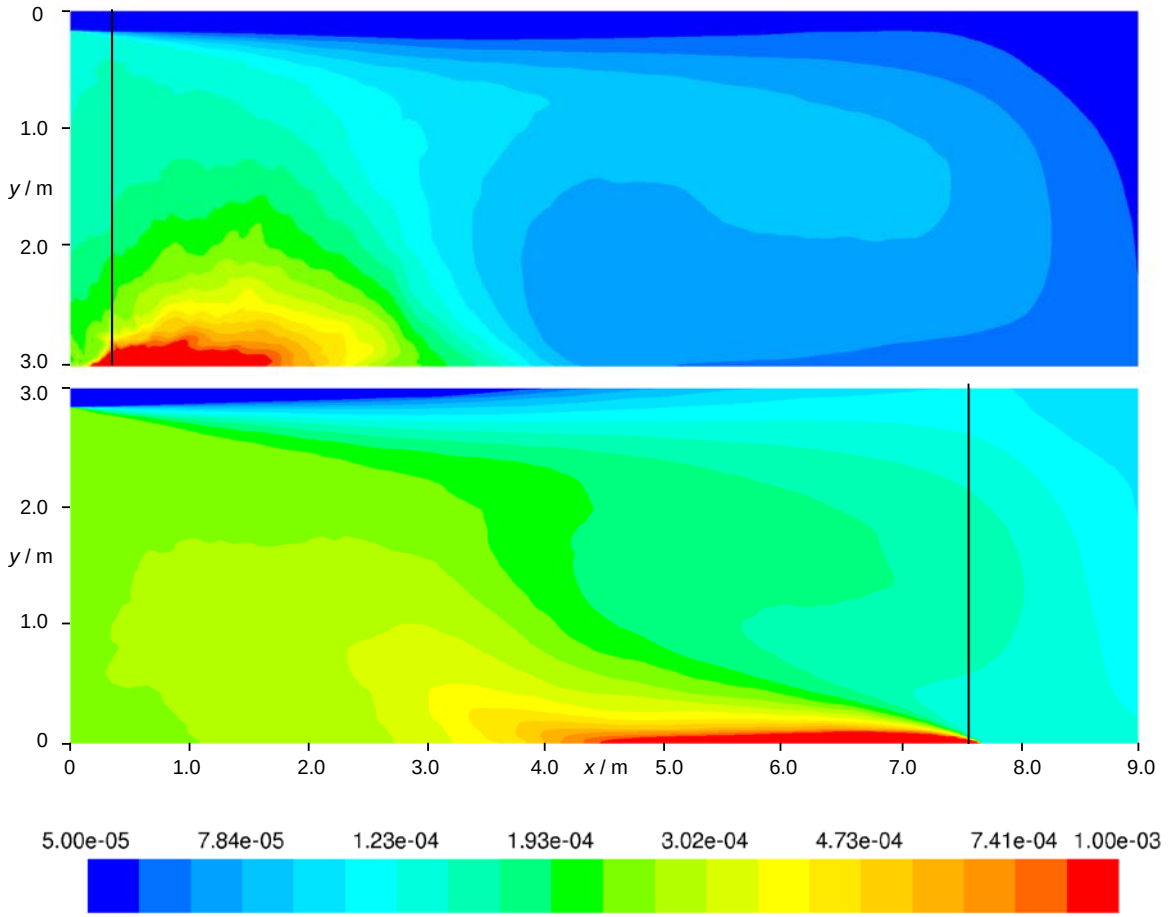

Fig. 6. Normalised mean concentrations ($\bar{c}/c_0$) for the large left source (upper) and the large right source (lower) on the vertical centre plane. The concentrations are shown on a log scale and are not clipped to the range. The vertical lines are positioned at the centres of the sources.

Fig. 7 and Fig. 8 show graphs of normalised mean concentration on vertical lines above the sources and downwind from the right source, and horizontal lines at various heights (Fig. 2 shows the locations of the lines). Lines VL1 and VR1 show how the mean concentration reduced rapidly over a short distance from the source. Within approximately 0.1 m or less from the sources in the vertical direction the concentrations have reduced by more than three or four orders of magnitude. For horizontal distances from the left sources (Fig. 8) greater than 4.5 m, $\bar{c}/c_0$ is almost constant at approximately 6.7 x 10^{-4} for the large source and a factor of 6.3 less for the small source, irrespective of the height of the horizontal line. For the right sources the downstream concentration decay in the horizontal direction is rapid. However, concentrations do not quite reach the background levels seen upwind of the source by the time the vapour plume reaches x = 0 m. The mean concentration profile flattens with increasing vertical or horizontal distance from the source. For a source of TNT, the background concentrations in the room would be approximately 0.22 part per trillion (ppt) and 0.036 ppt for the left large and small source respectively and 0.44 ppt and 0.070 ppt for the right large and small source respectively.

As would be expected from their relative vapour fluxes, the time-averaged concentrations from the large sources were consistently 6.3 times that from the small sources (calculated along the lines in both the horizontal and vertical directions), apart from very close to the source.

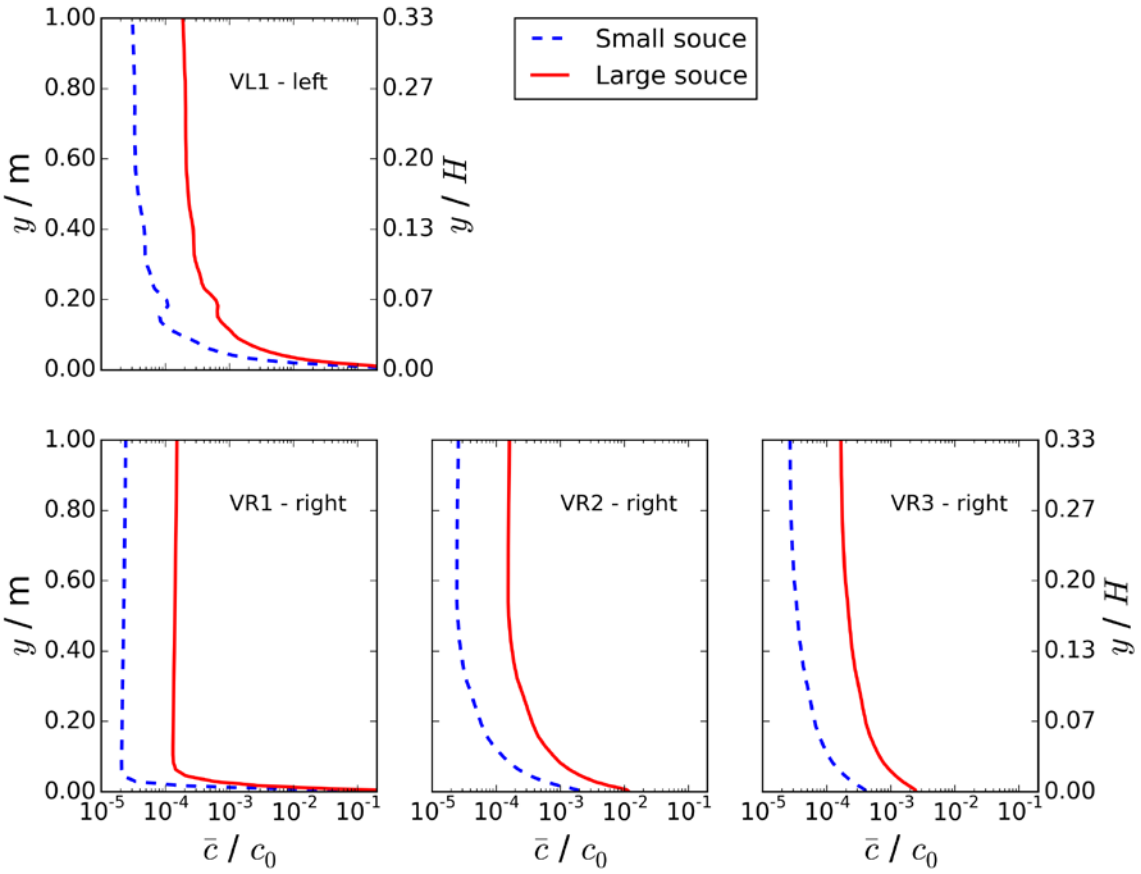

497

498 Fig. 7. $\bar{c}/c_0$ along vertical lines VL1, VR1, VR2 and VR3. The upper graph shows releases from the left sources
499 and the lower graphs the right sources. Only data up to y = 1.0 m (or y / H = 0.33) is shown.

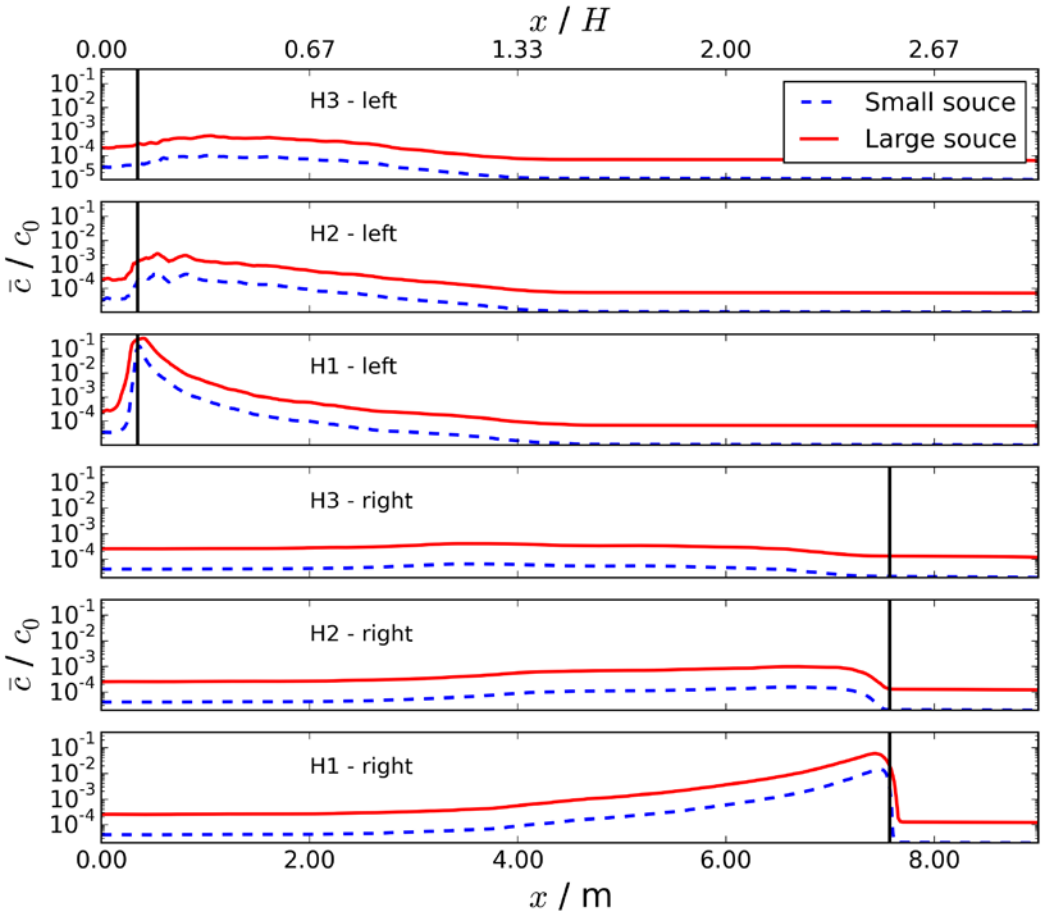

Fig. 8. $\bar{c}/c_0$ along horizontal lines H3, H2 and H1. The upper three graphs show releases from the left sources and the lower three graphs the right sources. The vertical black lines indicate the location of the centre of the sources.

To illustrate the intensity of the fluctuating concentration (as would be used in eddy chemotaxis), Fig. 9 and Fig. 10 show the RMS of the fluctuating concentration relative to the local mean concentration, $c_{RMS}/\bar{c}$. There is little difference between $c_{RMS}/\bar{c}$ for the two source sizes apart from in the near-source region and a small region to the left of the left sources on line H1. This shows that generally the intensity of the relative concentration fluctuations is not sensitive to the source size for these two sizes. For the right sources there is a clear gradient in the upwind direction leading to the source. This is similar to that of a ground level source in an atmospheric boundary layer flow [21, 22, 28]. For the left sources, the pattern of the gradient is complex but there is a clear gradient upwind of the left source (on the left of the room). The results for the right source can be compared quantitatively to published data from wind tunnel and LES studies of ground level passive scalar releases in a fully turbulent boundary layer. On the horizontal line 0.01 m above the floor, H1, $c_{RMS}/\bar{c}$ peaks between 1.4 and 1.8 (downwind of the source) which is larger but within a factor of four of the published data (0.8 [22], 0.5 [21], 0.5 [28]). It should be noted that the boundary layer in the scenario studied here is unlikely to be fully developed.

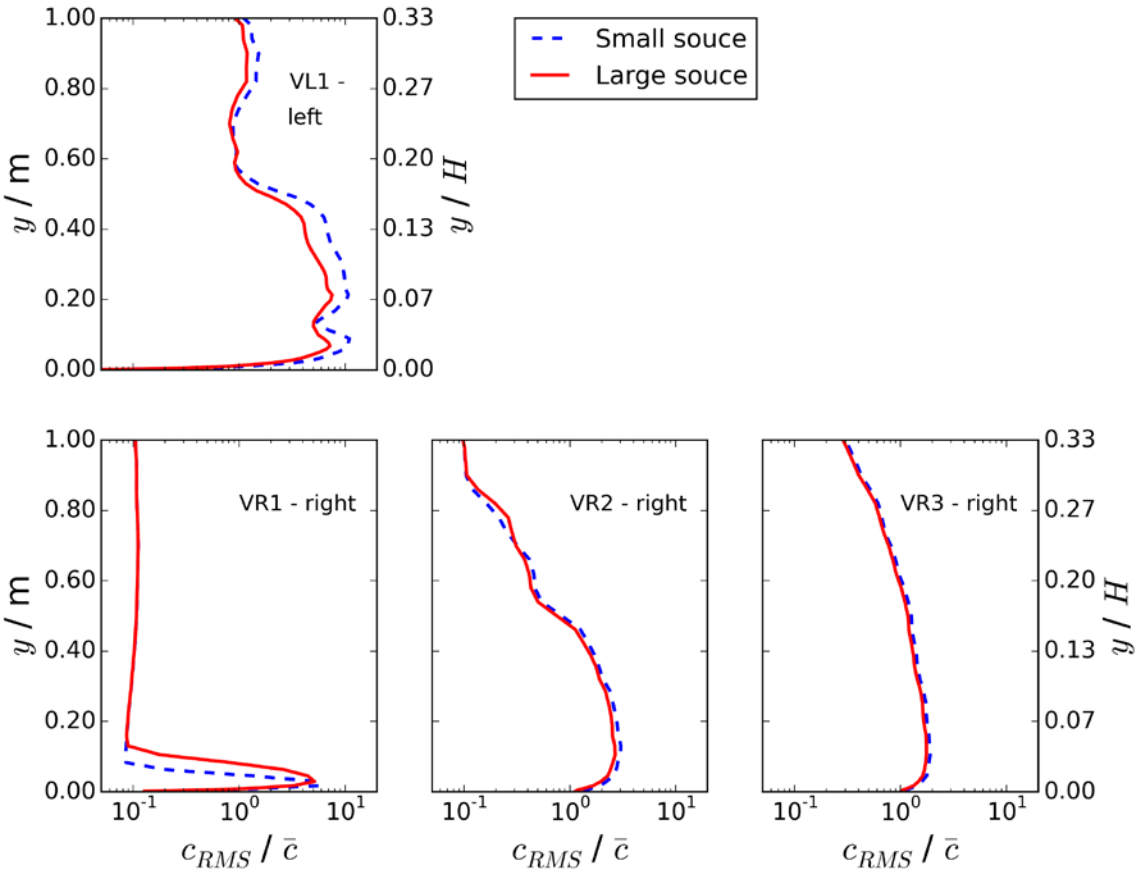

Fig. 9. $c_{RMS}/\bar{c}$ along vertical lines VL1, VR1, VR2 and VR3. The upper graph shows releases from the left sources and the lower graphs the right sources. Only data up to y = 1.0 m (or y / H = 0.33) is shown.

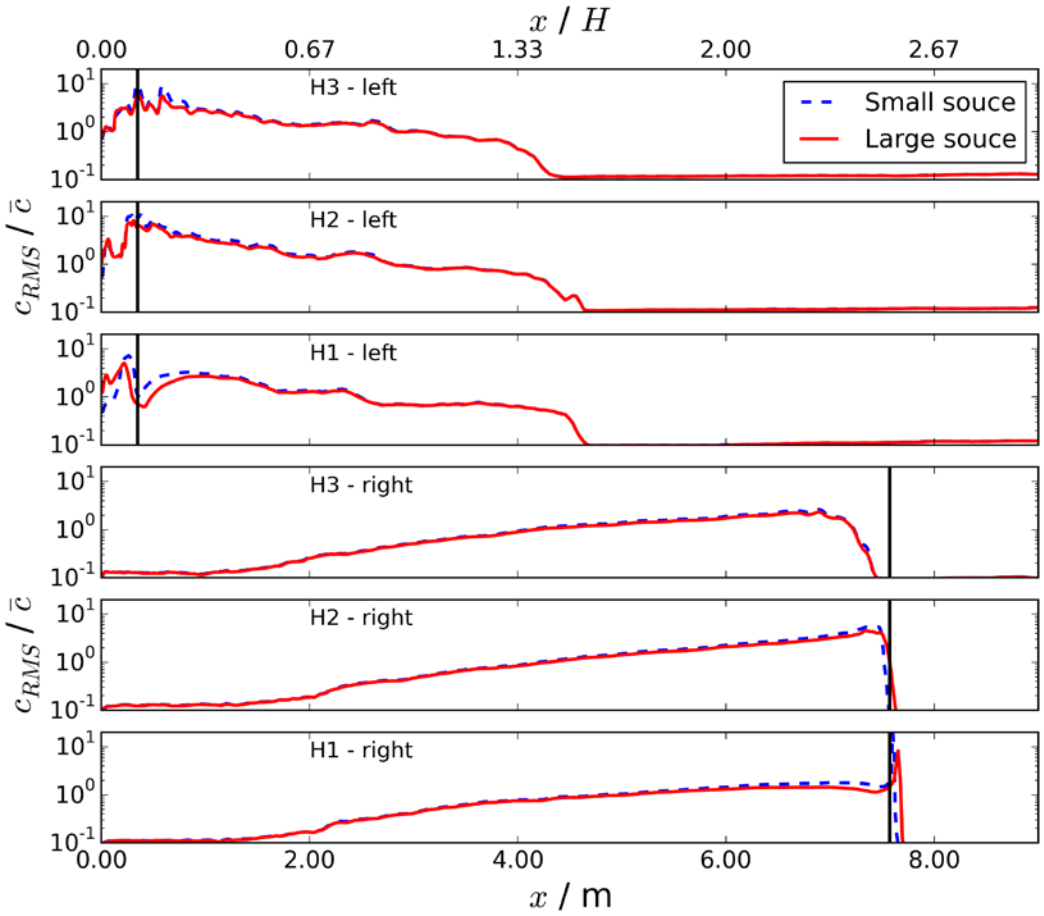

Fig. 10. $c_{RMS}/\bar{c}$ along horizontal lines H3, H2 and H1. The upper three graphs show releases from the left sources and the lower three graphs the right sources. The vertical black lines indicate the location of the centre of the sources.

Probability histograms of relative instantaneous concentrations, $c/\bar{c}$, are shown in Fig. 11 and Fig. 12 at the monitor points. The 99th percentile value for $c/\bar{c}$, C_{99th}, is given on each graph. The results at PL2 and PR2 were similar to PL3 and PR3 respectively so have not been included. For the left sources the largest value of C_{99th} was 28.1, which was for the large source at point PL1 (Fig. 12). It should be noted that similar results were produced in a test model with Δt = 0.01 s or 0.005 s. At point PL3, C_{99th} was approximately nine for both sources sizes. C_{99th} was 1.1 and 1.6 for both the small and large sources at PR1 and PR3 respectively.

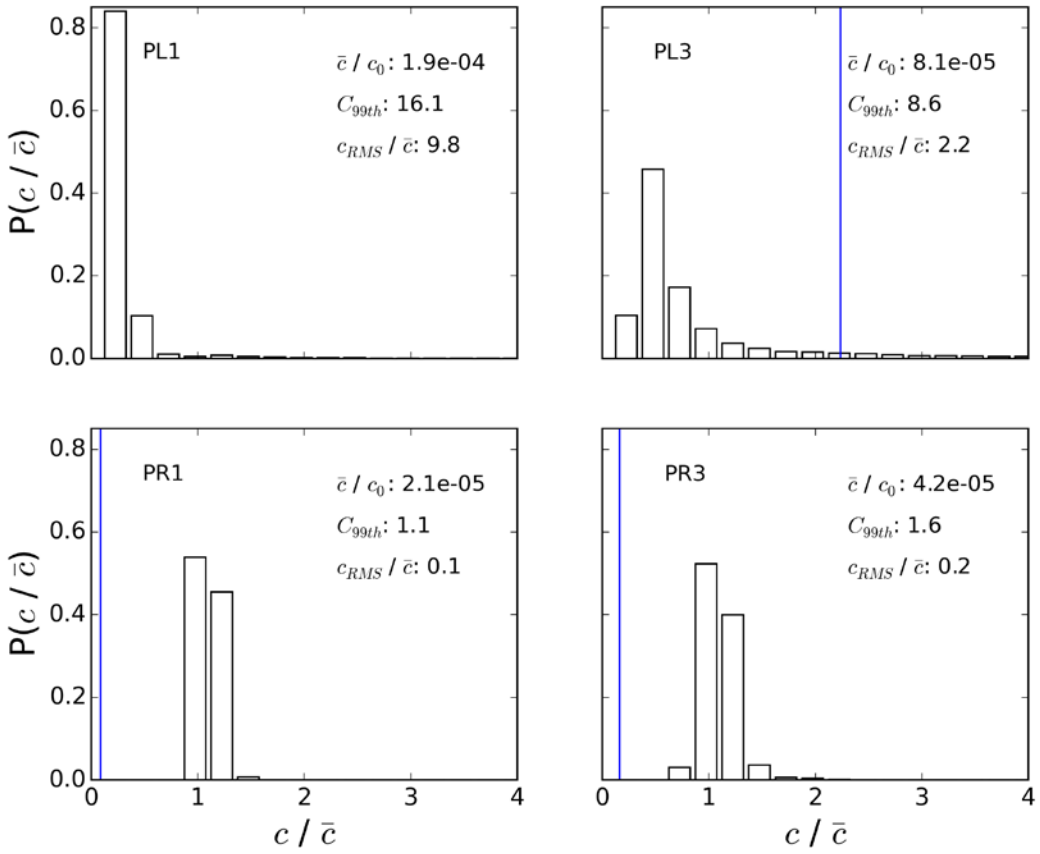

536

537 Fig. 11. The probability of $\boldsymbol{c/\bar{c}}$ for the small sources at points PL1, PL3, PR1 and PR3. The upper graphs show
538 releases from the left sources and the lower graphs the right sources. The vertical line shows $\boldsymbol{c_{RMS}/\bar{c}}$. The bin
539 width = 0.25.

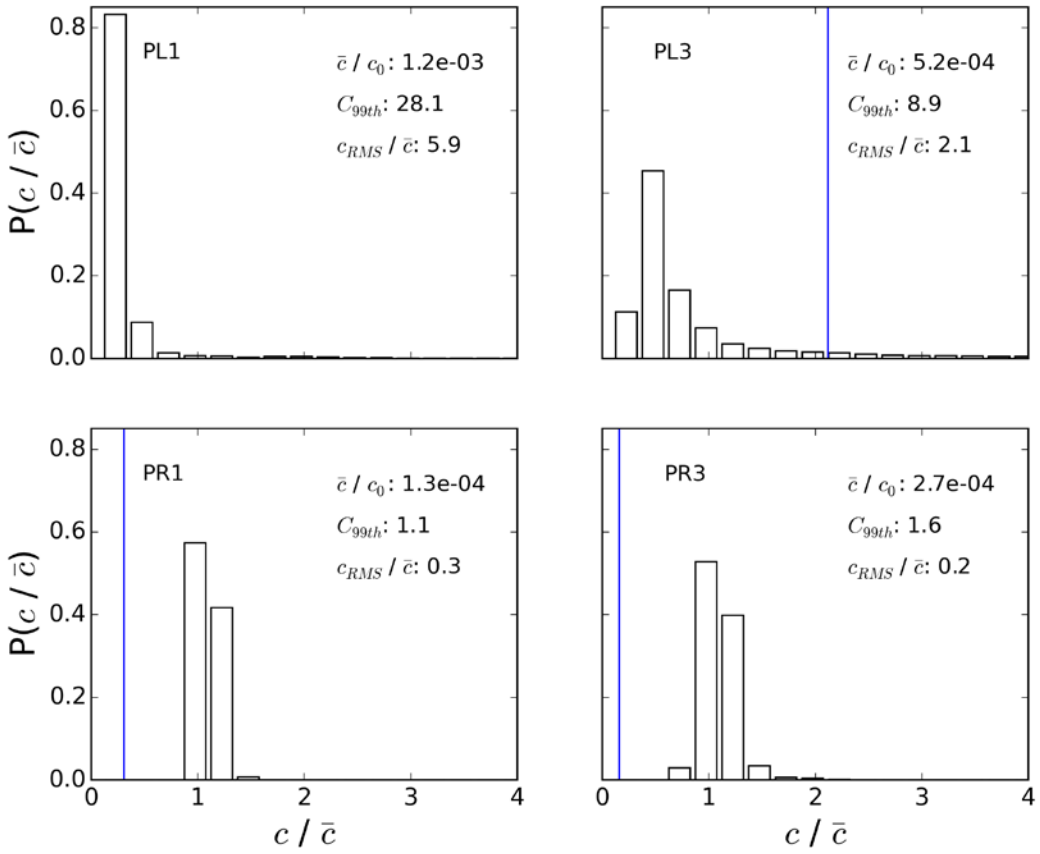

Fig. 12 The probability of $\boldsymbol{c/\bar{c}}$ for the large source at points PL1, PL3, PR1 and PR3. The upper graphs show releases from the left sources and the lower graphs the right sources. The vertical line shows $\boldsymbol{c_{RMS}/\bar{c}}$. The bin width = 0.25.

Time histories at a number of locations in the model showed that concentrations from both the small and large sources were almost identical when normalised with their respective time-average concentrations. This was the same for both source locations. The frequency of the concentration fluctuations was of the order of approximately 1 Hz or slower.

4. Relating the results to chemical location techniques and the detection of vapour using dogs

The following discussion is based on the specific geometry and flow studied. Therefore, the conclusions cannot necessarily be applied to other types of room. However, the same principles should apply in appropriate cases. As stated previously, the primary aim of this study is to investigate the unsteady flow present in rooms and the extent to which it can produce complex vapour fields that could either help or hinder vapour detection. Secondly, the intention is to illustrate some of the key features of these vapour fields to raise the awareness of people conducting either training or operational detection activities.

Depending on the limit of detection of the dog and the source of the vapour, the animal may not be aware of the vapour until it enters the high concentration region, immediately adjacent to the source, due to the diluting effect of the supplied fresh air. This would be particularly relevant for low volatility materials, e.g. most explosives and some toxic liquids. Based on a dog's sampling frequency, up to 7 Hz [36], it should be able to detect the concentration fluctuations. The instantaneous concentrations could be greater than 28 times the mean when sampling 0.1 m from the source and greater than 8 times at more than 1 m from the source. This effect was reduced for the right source as the flow there was less unsteady than at the left source. These peak concentrations were only present for 1% of the time and the peaks were typically more than a minute apart. Therefore, a dog may need to remain stationary or to continue to search within a region in order to come across them.

Assuming that a dog can detect the vapour, consideration should be made for how it could then track to the source location. For both release locations there was a mean concentration gradient (in both the vertical and horizontal directions) leading towards the source. Therefore, chemotaxis may be a suitable method to track towards a vapour source in these cases. It should be noted that the unsteady nature of the vapour field means that a dog would need to be stationary and sampling the air for an unreasonably long period of time (of the order of τ, i.e. 353 s) to be able to sense (and then utilise) the time-averaged concentration field. This point should also be of interest to those designing autonomous sensor systems for operation indoors. It may be that dogs or autonomous systems could use eddy chemotaxis due to relatively low frequency of the concentration fluctuations. Due to the way air circulates in rooms it is possible that the source of an odour could lay downwind of the location where a dog first detects a signal. As a result anemotaxis would also not be expected to work in all cases. All sources produced a relative RMS concentration field in which magnitudes decreased with distance from the source. The horizontal gradient was mainly contained within the left of the room for the left sources. To find the source of vapour the dog may have to employ a structured (e.g. the spiral search pattern of Ferri et al. [2]) or random search pattern to enable it to move into the high concentration/gradient region near the source.

As mentioned earlier, the movement of a dog and handler in the room has not been accounted for in the modelling but it is expected that this movement would produce additional unsteadiness and increase local mixing.

The large vapour sources, with nine times the surface area of the small sources, only produced concentration 6.3 times higher. This was because the flux, F, from the large sources was 0.7 times that of the small sources. This has implications for the use of source materials in training exercises; increasing the surface area of the source may not increase the vapour concentration in the room proportionally.

The RMS concentration and the instantaneous concentration (not shown in this paper) relative to the local time-averaged concentration were almost indistinguishable between the two sources, except very close to the source. Fackrell and Robins [21] saw a similar effect for ground level sources in their wind tunnel study. They pointed out that the key ratio was the local turbulence integral length scale to the source diameter. When the local integral length scale is smaller than the source, the relative RMS concentration should be independent of source size. The implication of this is that small sources of explosive should produce the same relative RMS and relative instantaneous concentration as a large source. However, this

would only apply when both sources are larger than the local integral length scale and within certain size constraints.

It would be interesting to test the above findings for rooms with typical ventilation strategies such as naturally ventilated spaces with non-iso-thermal conditions. The effects of vapour sorption should also be considered as the low vapour pressure of most materials of interest means that they will partition onto surfaces very readily.

5. Conclusions and discussion

An LES CFD model of vapour transport from a constant concentration source in a mechanically ventilated room has been used to illustrate the capability of LES to simulate the complexity of indoor vapour fields and to assess how they relate to detection using dogs.

The predicted turbulence statistics up to the 2nd order moment are generally in agreement with experimental data [39] (FAC2 of 0.75 and 0.95 and FAC1.3 of 0.53 and 0.51 for mean and RMS velocity respectively). Other studies (e.g. [45, 46]) have captured certain flow features better than achieved here, but the use of LES has enabled the fluctuating velocity field to be predicted more accurately than in studies using a RANS approach. There are some uncertainties over the experimental data [39], for example, it was not reported what the conditions upstream of the inlet were. However, the modelled flow was not particularly sensitive to the level of turbulence applied at the inlet. There is some question over the two-dimensionality of the flow [45, 51, 52] and Nielsen [51] stated that it is possible that different flow patterns were present in the experiment but were not captured in the reported data. This means that there may be more than one correct solution for the flow, as can be the case for room airflows [8, 51], where the flow can switch between different stable modes. Regarding the model setup, there are a considerable number of components in an LES model that can be selected by the user. While great effort has been made to assess the sensitivity to the key ones, it is not practical to assess them all. For example, it is not known whether a finer mesh across the domain with a second order central difference scheme applied to the species transport equations would improve the accuracy of the peak concentration predictions. However, best practice, based on previously reported studies, was used to define the modelling approach. Finally, the predicted scalar flux and intensity of concentration fluctuations were compared against analytical models and wind tunnel and LES data in the literature with success.

Due to the low volatility of some compounds of interest and the diluting effect of the fresh air in the room, the time averaged vapour concentrations present in the bulk of the room may be extremely low, whereas the peak concentration can be much greater than the mean. Near the source the concentrations fluctuate significantly but the amplitude of these fluctuations was shown to be dependent on the location of the source, and the local turbulent flow field. We found that instantaneous concentrations of approximately 28 times the mean were predicted 0.1 m away, and greater than 8 times the mean more than 1 m away for the large and small left sources. These peaks were present for 1% of the time.

The vapour field does not scale linearly with the surface area of the source, for the modelled source sizes. This is perhaps not surprising given the very low speed of airflow in the room and the relatively large area size of the sources. Also, the source size did not have a significant effect on the instantaneous and RMS concentrations, relative to the local mean concentration, apart from close to the source. Therefore, ten times the surface area of the source material would not produce ten times the vapour, but may produce the same relative RMS and relative instantaneous concentration field.

Based on the ways in which animals are known to use air- or water-borne chemicals to locate a source, it is not clear whether there is sufficient information present in large parts of the room for dogs to be able to achieve this after they have detected the vapour. It may be necessary to use a structured or random search pattern that enables the dog to encounter sufficiently high concentrations or gradients (in the mean or RMS field) close to the source.

The conclusions above are based on a simple indoor scenario and although the findings cannot be directly extrapolated to others types of room, the same principles should apply in appropriate cases. The methods developed in this study could be applied to a range of room types, including various mechanical ventilation configurations, and various room shapes.

Acknowledgements

The research was supported by the UK Ministry of Defence and the PhD scheme in the Faculty of Engineering and the Environment at the University of Southampton.

References

1. Zhai Z., Zhang Z., Zhang W., Chen Q. Evaluation of various turbulence models in predicting airflow and turbulence in enclosed environments by CFD: part 1- summary of prevalent turbulence models. HVAC&R Res. 13 (2007) 853-870.
2. Ferri G., Caselli E., Mattoli V., Mondini A., Mazzolai B., Dario P. SPIRAL: A novel biologically-inspired algorithm for gas/odor source localization in an indoor environment with no strong airflow. Robot. Auton. Syst. 57 (2009) 393-402.
3. Chen, Q. Ventilation performance prediction for buildings: A method overview and recent applications, Build. Environ. 44 (2009) 848–858.
4. Restivo A. Turbulent flow in ventilated rooms, PhD thesis. University of London; 1979.
5. Zhang Z., Chen X., Mazumdar S., Zhang T., & Chen Q. Experimental and numerical investigation of airflow and contaminant transport in an airliner cabin mockup. Build. Environ. 44 (2009) 85-94.
6. Linden P. F. The fluid mechanics of natural ventilation. Annu. Rev. Fluid Mech. 31 (1999) 201-238.
7. Axley J. Multizone airflow modeling in buildings: History and theory. HVAC&R Res. 13 (2007) 907-928.
8. Li, Y., Nielsen, P.V. CFD and ventilation research. Indoor Air 21 (2011) 442-453.
9. Nielsen, P. V. Fifty years of CFD for room air distribution. Build. Environ. 91 (2015) 78-90.
10. Zhang Z., Zhang W., Zhai Z.J., Chen, Q.Y. Evaluation of various turbulence models in predicting airflow and turbulence in enclosed environments by CFD: Part 2—Comparison with experimental data from literature. HVAC&R Res. 13 (2007) 871-886.
11. van Hooff T., Blocken B., Gousseau P., van Heijst G.J.F. Counter-gradient diffusion in a slot-ventilated enclosure assessed by LES and RANS. Comput. Fluids 96 (2014) 63–75.

12. Endregard M., Reif B.A.P., Vik T., Busmundrud O. Consequence assessment of indoor dispersion of sarin—A hypothetical scenario. J. Hazard. Mater. 176 (2010) 381-388.
13. Choi J.I., Edwards J.R. Large-eddy simulation of human-induced contaminant transport in room compartments. Indoor air 22 (2012) 77-87.
14. Drescher A.C., Lobascio C., Gadgil A.J., Nazaroff W.W. Mixing of a point-source indoor pollutant by forced convection, Indoor Air 5 (1995) 204-214.
15. Cheng K-C., Acevedo-Bolton V., Jiang R-T., Klepeis N.E., Ott W.R., Fringer O.B., Hildemann L.M. Modeling Exposure Close to Air Pollution Sources in Naturally Ventilated Residences: Association of Turbulent Diffusion Coefficient with Air Change Rate, Environ. Sci. Technol. 45 (2011) 4016–4022.
16. Topp C. Diffusion and evaporation-controlled emission in ventilated rooms. PhD thesis. Aalborg University; 1999.
17. Acevedo-Bolton V., Cheng K-C., Jiang R-T., Ott W.R., Klepeis N.W., Hildemann L.M. Measurement of the proximity effect for indoor air pollutant sources in two homes. J. Environ. Monit. 14 (2012) 94-104.
18. Hargather M.J., Staymates M.E., Madalis M.J., Smith D.J., & Settles G.S. The Internal Aerodynamics of Cargo Containers for Trace Chemical Sampling and Detection. IEEE Sens. J. 11 (2011) 1184-1193
19. Ong T. H., Mendum T., Geurtsen G., Kelley J., Ostrinskaya A., Kunz R.. Use of Mass Spectrometric Vapor Analysis to Improve Canine Explosive Detection Efficiency. Anal. Chem. 89 (2017) 6482-6490
20. Tominaga Y., Blocken B. Wind tunnel analysis of flow and dispersion in cross-ventilated isolated buildings: impact of opening positions. J. Wind Eng. Ind. Aerod. 31 (2016) 74-88.
21. Fackrell J.E., Robins A.G. Concentration fluctuations and fluxes in plumes from point sources in a turbulent boundary layer. J. Fluid Mech. 117 (1982) 1-26.
22. Xie Z-T., Hayden P., Robins A.G., Voke P.R. Modelling extreme concentrations from a source in a turbulent flow over a rough wall. Atmos. Environ. 41 (2007) 3395–3406.
23. Xie Z.T., Castro I.P. Large-eddy simulation for flow and dispersion in urban streets. Atmos. Environ. 43 (2009) 2174-85.
24. Boppana V.B.L., Xie Z-T., Castro I.P. Large-eddy simulation of dispersion from surface sources in arrays of obstacles. Bound-Lay. Meteorol. 135 (2010) 433-454.
25. Gousseau P., Blocken B., Van Heijst G.J. CFD simulation of pollutant dispersion around isolated buildings: On the role of convective and turbulent mass fluxes in the prediction accuracy. J. Hazard. Mater. 194 (2011) 422-434.
26. Salim S.M, Buccolieri R., Chan A., Di Sabatino S. Numerical simulation of atmospheric pollutant dispersion in an urban street canyon: Comparison between RANS and LES. J. Wind Eng. Ind. Aerod. 99 (2011) 103-113.
27. Tominaga Y., Stathopoulos T. CFD modeling of pollution dispersion in a street canyon: Comparison between LES and RANS. J. Wind Eng. Ind. Aerod. 99 (2011) 340-8.
28. Boppana V.B.L, Xie Z-T., Castro I.P. Large-eddy simulation of dispersion from line sources in a turbulent channel flow. Flow Turbul. Combust. 88 (2012) 311–342.
29. Kauhanen E., Harri M., Nevalainen A., Nevalainen T. Validity of detection of microbial growth in buildings by trained dogs. Environ. Int. 28 (2002) 153-157.
30. Arner L. D., Johnson G. R., Skovronek H. S. Delineating toxic areas by canine olfaction. J. Hazard. Mater. 13 (1986) 375-381.
31. Furton K. G., Myers L. J. The scientific foundation and efficacy of the use of canines as chemical detectors for explosives. Talanta 54 (2001) 487-500.

32. Habib M.K. Controlled biological and biomimetic systems for landmine detection. Biosens. Bioelectron. 23 (2007) 1-18.
33. Vickers N.J. Mechanisms of animal navigation in odor plumes. Biol. Bull. 198 (2000) 203–212.
34. Weissburg M.J. The fluid dynamical context of chemosensory behavior. Biol. Bull. 198 (2000) 188–202.
35. Atema J. Eddy chemotaxis and odor landscapes: exploration of nature with animal sensors. Biol. Bull. 191 (1996) 129-138.
36. Craven B.A, Paterson E.G., Settles G.S. The fluid dynamics of canine olfaction: unique nasal airflow patterns as an explanation of macrosmia. J. R. Soc. Interface 7 (2010) 933–943.
37. Craven B.A. A fundamental study of the anatomy, aerodynamics, and transport phenomena of canine olfaction. PhD thesis, The Pennsylvania State University; 2008.
38. Finkelstein W., Melikov A., Sefker T., and Langkilde G. Laser doppler measurement of air flow characteristics in rooms with mechanical ventilation. Indoor Air 96. Proceedings of the 7th international conference on indoor air quality and climate; 1996
39. Nielsen P.V. Specification of a two-dimensional test case: (IEA). Aalborg: Institut for Bygningsteknik, Aalborg Universitet, (Gui serie; No. 8, R9040); 1990.
40. Chen Q. Comparison of different k-ε models for indoor air flow computations. Numerical Heat Tr. B-Fund. 28 (1995) 353-69.
41. Rong L., Nielsen P.V. Simulation with different turbulence models in an annex 20 room benchmark test using Ansys CFX 11.0. Aalborg University. ISSN 1901-726X; 2008.
42. Susin R.M., Lindner G.A., Mariani V.C., Mendonça K.C. Evaluating the influence of the width of inlet slot on the prediction of indoor airflow: comparison with experimental data. Build. Environ. 44 (2009) 971–986.
43. Le Dreau J., Heiselberg P.K., Nielsen P.V. Simulation with different turbulence models in an annex 20 benchmark test using Star-CCM+. Aalborg: Department of Civil Engineering, Aalborg University. (DCE technical reports; No. 147); 2012.
44. Pulat E., Ersan, H. A. Numerical simulation of turbulent airflow in a ventilated room: Inlet turbulence parameters and solution multiplicity. Energ. Buildings 93 (2015) 227-235.
45. Thysen J-H. CFD analysis of the mixing in an enclosure under time-periodic inlet conditions (Thesis). Eindhoven University of Technology (2015). Retrieved from https://pure.tue.nl/ws/files/46924660/841501-1.pdf.
46. Davidson L. Implementation of a large-eddy simulation method applied to recirculating flow in a ventilated room. Aalborg: Dept of Building Technology and Structural Engineering, Aalborg University. (Gui serie; No. 30, Vol. R9611); 1996.
47. Muller D., Davidson L. Comparison of different subgrid turbulence models and boundary conditions for large-eddy-simulation of room air flows. H.B. Awbi (Ed.), Proc. Roomvent, Elsevier Science Ltd, Amsterdam, 2000, pp. 301-306.
48. Voigt L.K. Navier-Stokes simulation of airflow in rooms and around a human body (Thesis). Technical University of Denmark (2001).
49. Zhang W., Chen Q. Large eddy simulation of indoor airflow with a filtered dynamic subgrid scale model. International J Heat Mass Tran. 43 (2000) 3219-3231.
50. Elhadidi B., Khalifa H.E. Comparison of coarse grid lattice Boltzmann and Navier Stokes for real time flow simulations in rooms. Build. Simul. 6 (2013) 183–194.
51. Nielsen P.V., Rong L., Cortes IO. The IEA Annex 20 two-dimensional Benchmark Test for CFD Predictions. In Clima 2010 : 10th Rehva World Congress: Sustainable Energy Use in Buildings. Antalya: Clima 2010 : 10th Rehva World Congress; 2010.

52. Voigt L.K. Evaluating turbulence models for 3-D flows in enclosure by topology, Montreal Canada: Ninth International IBPSA Conference; 2005
53. ANSYS. ANSYS FLUENT 15.0 Theory Guide, ANSYS Inc. 2013.
54. Liu C. H., Barth M. C. Large-eddy simulation of flow and scalar transport in a modeled street canyon. Journal Appl. Meteorol. 41 (2002) 660-673.
55. Gousseau P., Blocken B., Stathopoulos T., van Heijst G.F. Near-field pollutant dispersion in an actual urban area: analysis of the mass transport mechanism by high-resolution Large Eddy Simulations. Comput. Fluids. 2 (2015) 151-62.
56. Xie Z-T., & Castro I.P. Efficient generation of inflow conditions for large eddy simulation of street-scale flows. Flow Turbul. Combust. 81 (2008) 449-470.
57. Aboshosha H., Elshaer A., Bitsuamlak G.T., El Damatty A. Consistent inflow turbulence generator for LES evaluation of wind-induced responses for tall buildings. J. Wind Eng. Ind. Aerod. 142 (2015) 198-216.
58. Panigrahi P.K., Acharya S. The flow over a surface mounted rib turbulator under single-mode and dual-mode excitation. J. Wind Eng. Ind. Aerod. 92 (2004) 1219-1244.
59. Pope S. Ten questions concerning the large-eddy simulations of turbulent flows. New J. Phys. 6 (2004) 1–24.
60. Abdilghanie A.M., Collins L.R., Caughey D.A. Comparison of turbulence modeling strategies for indoor flows. J Fluid Eng. 131 (2009).
61. Liu Z., Yea W., Little J.C. Predicting emissions of volatile and semivolatile organic compounds from building materials: A review. Build. Environ. 64 (2013) 7-25.
62. Gershanik A., Zeiri Y. Sublimation rate of TNT microcrystals in air. J. Phys. Chem. A 114 (2012) 12403-12410.
63. Ostmark H., Wallin S., Ang H.G. Vapor pressure of explosives: a critical review. Propellants Explos. Pyrotech. 37 (2012) 12-23.
64. Danberg J.E., Evaporation into Couette flow. Edgewood ECBC-CR-092; 2008.
65. Pedersen J., Meyer K. POD analysis of flow structures in a scale model of a ventilated room. Exp. Fluids 33 (2000) 940-949.
66. Hanna S.R., Hansen O.R., Dharmavaram S. FLACS CFD air quality model performance evaluation with Kit Fox, MUST, Prairie Grass, and EMU observations. Atmos. Environ. 38 (2004) 4675-87.
67. Tominaga Y. Flow around a high-rise building using steady and unsteady RANS CFD: Effect of large-scale fluctuations on the velocity statistics. J. Wind Eng. Ind. Aerod. 142 (2015) 93-103.
68. van Hooff T., Blocken B., Tominaga Y. On the accuracy of CFD simulations of cross-ventilation flows for a generic isolated building: comparison of RANS, LES and experiments. Build. Environ. 114 (2017) 148-65.